Modeling and Design of 3D printed Hyperelastic Lattice Metamaterials with Bionic S-shaped Stress-strain Behaviors

Le Dong[a,b], Mengjie Zhang[a,b] and Dong Wang[a,b,*]

[a] *State Key Laboratory of Mechanical System and Vibration, School of Mechanical Engineering, Shanghai Jiao Tong University, Shanghai 200240, China*

[b] *Shanghai Key Laboratory of Intelligent Robotics, Meta Robotics Institute, Shanghai Jiao Tong University, Shanghai 200240, China*

File List

*Corresponding author
wang_dong@sjtu.edu.cn (D. Wang)

1. Internal and external forces in discretization formulation

Combining Eqs. (14) and (15), the variation of the strains can be expressed by the shape functions as

$$\delta\boldsymbol{\varepsilon}_{\mathbf{e}} = \sum_{I=1}^{3} \mathbf{B}_I \delta\mathbf{u}_I \text{ with } \mathbf{B}_I = \begin{bmatrix} N'_I\cos\psi_e & N'_I\sin\psi_e & \alpha_e N_I \\ -N'_I\sin\psi_e & N'_I\cos\psi_e & \beta_e N_I \\ 0 & 0 & N'_I \end{bmatrix}, \tag{S1}$$

where $\alpha_e = -\left(1 + u'_e\right)\sin\psi_e + w'_e\cos\psi_e$ and $\beta_e = -\left(1 + u'_e\right)\cos\psi_e - w'_e\sin\psi_e$. The virtual strain energy of the element Π_{int} and the virtual work of external loads acting on that element Π_{ext} can be obtained as follows

$$\begin{cases} \delta\Pi_{\text{int}} = \displaystyle\int_0^{l_e} (N\delta\varepsilon + Q\delta\gamma + M\delta\kappa)\, dx = \int_0^{l_e} \delta\boldsymbol{\varepsilon}_{\mathbf{e}}^{\mathrm{T}}\mathbf{S}_{\mathbf{r}} dx, \\ \delta\Pi_{\text{ext}} = \displaystyle\int_0^{l_e} (n\delta u + q\delta w + m\delta\psi)\, dx \\ \qquad + \displaystyle\sum_{I=1}^{3} \left(n_I\delta u_I + q_I\delta w_I + m_I\delta\psi_I\right) \\ \qquad = \displaystyle\int_0^{l_e} \delta\mathbf{u}_{\mathbf{e}}^{\mathrm{T}}\mathbf{q} dx + \sum_{I=1}^{3} \delta\mathbf{u}_I^{\mathrm{T}}\mathbf{q}_I. \end{cases} \tag{S2}$$

where $\mathbf{q} = \{n, q, m\}$ and $\mathbf{q}_I = \left\{n_I, q_I, m_I\right\}$. n, q and m are the axial and perpendicular external loads and moment per unit length, respectively. n_I, q_I and m_I stand for the point force and moment, respectively. Eq. (S2) is integrated along the beam length in the current configuration Ω. Substituting Eq. (S1) into Eq. (S2) gives

$$\begin{cases} \delta\Pi_{\text{int}} = \sum_{I=1}^{3} \delta\mathbf{u}_I^{\mathrm{T}} \int_0^{l_e} \mathbf{B}_I^{\mathrm{T}}\mathbf{S}_{\mathbf{r}} dx, \\ \delta\Pi_{\text{ext}} = \sum_{I=1}^{3} \delta\mathbf{u}_I^{\mathrm{T}}(\int_0^{l_e} N_I\mathbf{q} dx + \mathbf{q}_I). \end{cases} \tag{S3}$$

Thus, the internal and external forces are obtained by

$$\begin{cases} \mathbf{f}_{\text{int}\,I}^{\mathbf{e}} = \int_0^{l_e} \mathbf{B}_I^{\mathrm{T}}\mathbf{S}_{\mathbf{r}} dx, \\ \mathbf{f}_{\text{ext}\,I}^{\mathbf{e}} = \int_0^{l_e} N_I\mathbf{q} dx + \mathbf{q}_I. \end{cases} \tag{S4}$$

2. Tangent stiffness matrix in discretization formulation

For non-follower loading, the element stiffness matrix $\mathbf{K}^{\mathbf{e}}$ in Eq. (18) can be obtained by calculating the increment of the virtual strain energy based on linearization as

$$\begin{aligned} \Delta\delta\mathcal{W}_{\text{int}} = \sum_{I=1}^{3}\sum_{K=1}^{3} \delta\mathbf{u}_I^{\mathrm{T}} \\ \left[\int_0^{l_e} \mathbf{B}_I^{\mathrm{T}}\mathbf{D}\mathbf{B}_K\, dx + \int_0^{L_e} \left(N\mathbf{G}_{IK}^{N} + Q\mathbf{G}_{IK}^{Q}\right) dx\right] \Delta\mathbf{u}_K \end{aligned}. \tag{S5}$$

The matrices $\mathbf{G}_{IK}^{N}$ and $\mathbf{G}_{IK}^{Q}$ are given by

$$\begin{cases} \mathbf{G}_{IK}^{N} = \begin{bmatrix} 0 & 0 & -N'_I N_K\sin\psi_e \\ 0 & 0 & N'_I N_K\cos\psi_e \\ -N_I N'_K\sin\psi_e & N_I N'_K\cos\psi_e & \sigma_N \end{bmatrix}, \\ \mathbf{G}_{IK}^{Q} = \begin{bmatrix} 0 & 0 & -N'_I N_K\cos\psi_e \\ 0 & 0 & -N'_I N_K\sin\psi_e \\ -N_I N'_K\cos\psi_e & -N_I N'_K\sin\psi_e & \sigma_Q \end{bmatrix}. \end{cases} \tag{S6}$$

where

$$
\begin{cases} \sigma_N = N_I N_K(-(1+u'_e)\cos\psi_e - w'_e \sin\psi_e), \\ \sigma_Q = N_I N_K((1+u'_e)\sin\psi_e - w'_e \cos\psi_e). \end{cases} \tag{S7}
$$

Thus, the $\mathbf{K}^{\mathbf{e}}_{IK}$ is given by

$$
\mathbf{K}^{\mathbf{e}}_{IK} = \int_0^{l_e} \mathbf{B}_I^{\mathrm{T}} \mathbf{D} \mathbf{B}_K dx + \int_0^{l_e} \left(N\mathbf{G}^N_{IK} + Q\mathbf{G}^Q_{IK} \right) dx. \tag{S8}
$$

The overall tangent stiffness matrix of the microstructure is calculated by

$$
\mathbf{K}^{\mathbf{e}} = \bigcup_{e=1}^{n_e} \sum_{I=1}^{3} \sum_{K=1}^{3} \mathbf{K}^{\mathbf{e}}_{IK}. \tag{S9}
$$

3. Finite element analysis

The finite element analysis is conducted using the commercial software ABAQUS (SIMULIA, Providence, RI). In the material module, the hyperelastic properties are defined. 3-node quadratic hybrid beam elements (B22H) are used, and refined meshes are adopted to ensure computational accuracy. For the periodic boundary condition, the left boundary nodes of the lattice metamaterial are fixed, and a vertical displacement is applied to the right boundary nodes. For the non-periodic boundary condition, the left boundary nodes are pinned and allowed horizontal sliding, while vertical forces are applied to the right boundary nodes. All simulations are carried out in quasi-static mode using Abaqus/Standard.

4. Material selection

To achieve S-shaped stress-strain response in hyperelastic lattice metamaterials, the materials should have high stretchability and 3D printable. 3D printable elastomer is chosen to replicate the hyperelastic properties of biological tissues. Additionally, for sensing applications, electrical conductivity is necessary for resistive signal monitoring. Consequently, commercial UV-curable elastomer (65A, QIEFENG) and conductive silicone (3872, SINWE) are used.

5. 3D printing parameters

The DLP 3D printing is performed using the DLi 3DLP9000 UV projector with a resolution of 2560 Œ 1600 pixels, where each pixel measures 42 ţm Œ 42 ţm. The layer thickness is set to 50 ţm. The light intensity is 1.86 mW/cm^2 and the exposure time for each layer is 1.1 s. For the DIW process, a nozzle diameter of 0.3 mm is used, with a nozzle height of 0.15 mm, a layer height of 0.3 mm, an extrusion pressure of 200 kPa, and a printing speed of 5 mm/s.

6. Mechanical test procedures

Mechanical properties of hyperelastic lattice metamaterials are tested using a uniaxial material testing system (Instron 68SC2). The periodic boundary conditions are applied as follows. (1) Both the top and bottom nodes of the lattice metamaterial are fixed to sliders. (2) The sliders are mounted on custom smooth rails, which are secured in the universal testing machine (UTM) clamp, allowing horizontal movement. (3) The UTM is adjusted to restore the vertical length of the lattice metamaterial to its original state after forces removal. (4) The testing is conducted at a stretching speed of 10 mm/min. The resistance and displacement data are recorded during the tests. For non-periodic boundary conditions, the top and bottom nodes of the lattice metamaterial are fixed to immovable sliders.

7. Tailorable S-shaped stress-strain behaviors

The S-shaped stress-strain behavior of hyperelastic lattice metamaterials is characterized by a toe region (low stiffness) and a nonlinear region (high stiffness). By adjusting design parameters, the mechanical response can be controlled. Specifically, the curvature function $R(\alpha) = \alpha^A + 1/(\alpha + B)$ was used to design the microstructures. Decreasing A increases the degree of curvature in the microstructures, which expands the toe region while minimally affecting the nonlinear region (Fig. 5a). Increasing D enhances the structural stiffness, increasing the stiffness of the nonlinear region with only slight effects on the toe region (Fig. 5b). By tuning these parameters, the S-shaped stress-strain behavior can be tailored to replicate the mechanical properties of biological tissues (Fig. 5c-d).

8. Rapid inverse design optimization

To enable rapid inverse design optimization within the proposed framework, optimization methods combining machine learning and evolutionary algorithms can be applied. The process could be as follows: First, the proposed framework is used to build a database that captures the relationship between geometry parameters and the corresponding S-shaped stress-strain curves of hyperelastic lattice metamaterials. Next, machine learning models can be trained on this dataset to serve as surrogate models, enabling fast forward predictions of mechanical performance. Finally, the machine learning models are integrated into the fitness function evaluation within an evolutionary algorithm, which can identify the optimal design parameters that yield the desired mechanical properties. This approach can facilitate the rapid customization of lattice structures for sensor and robotic applications.

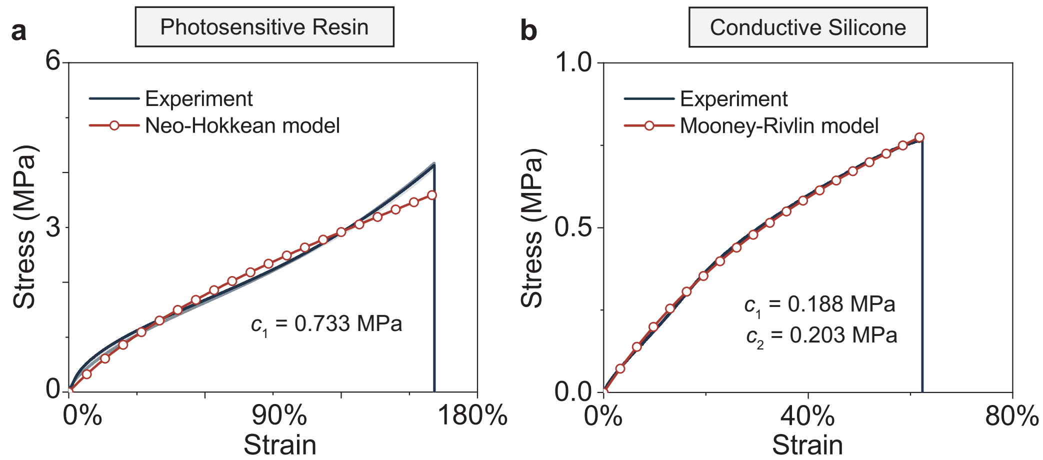

Figure S1: Material characterization. (a) Nominal stress-strain behaviors of photosensitive resin used for fabrication. The fitted material constant $c_1 = 0.733$ MPa with the neo-Hookean model. (b) Nominal stress-strain behaviors of conductive silicone for stretchable lattice conductors. The fitted material constants $c_1 = 0.188$ MPa and $c_2 = 0.203$ MPa with the Mooney-Rivlin model.

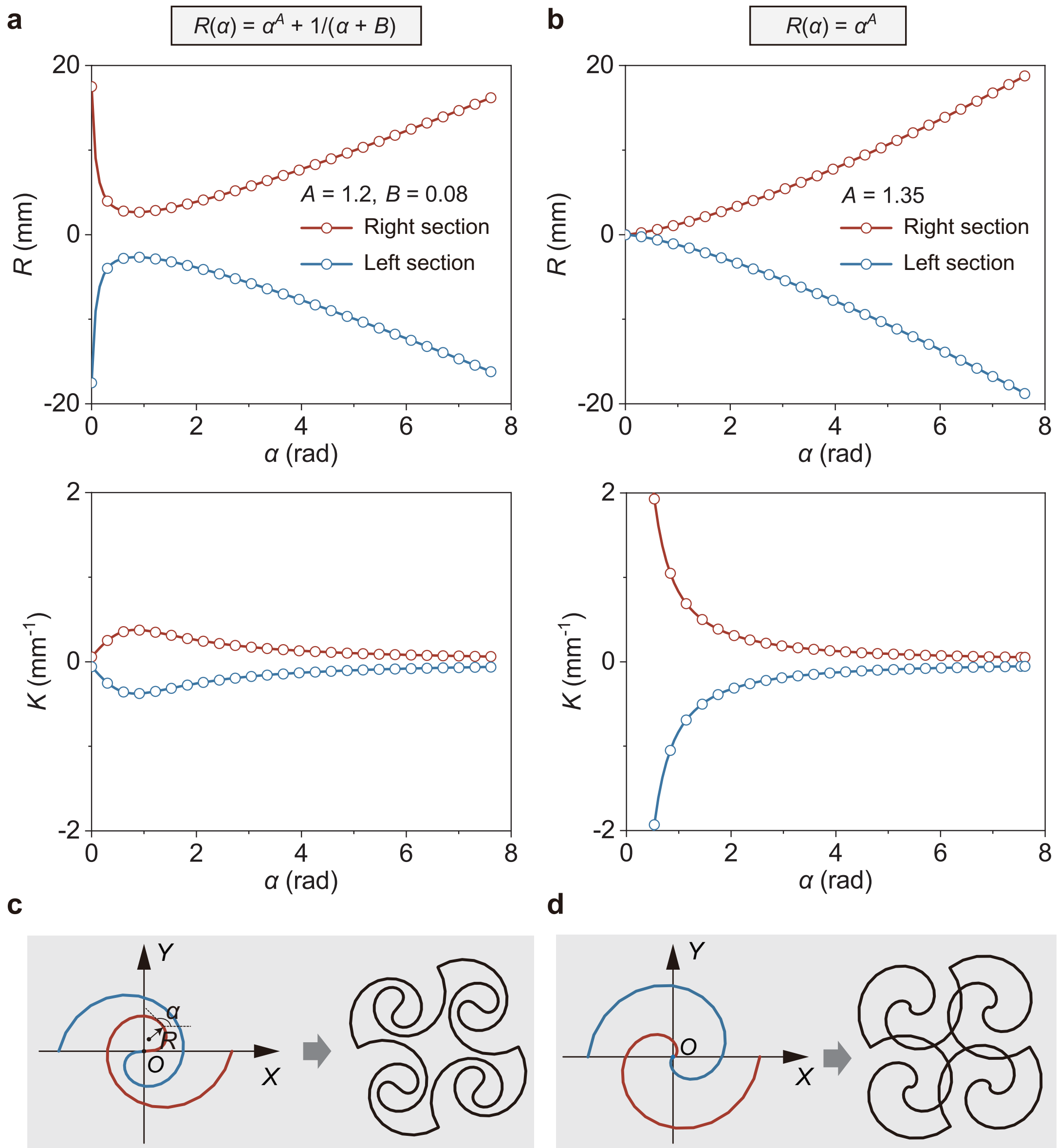

Figure S2: Geometry design. (a) Slope angle α versus instantaneous radius of curvature R and curvature K for the function (a) $R(\alpha) = \alpha^{\mathbf{A}} + 1/(\alpha + B)$ and (b) $R(\alpha) = \alpha^{A}$. (c) and (d) Corresponding microstructure and lattice unit geometries.

.

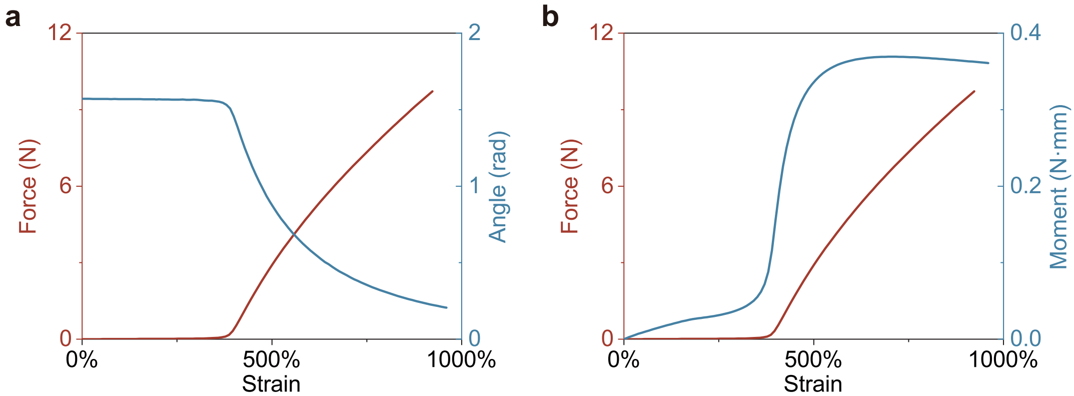

Figure S3: Mechanical behaviors under periodic boundary conditions. (a) Correlation between strain-force curves and strain-node angle change curves. (b) Correlation between strain-force curves and strain-applied moment curves.

.

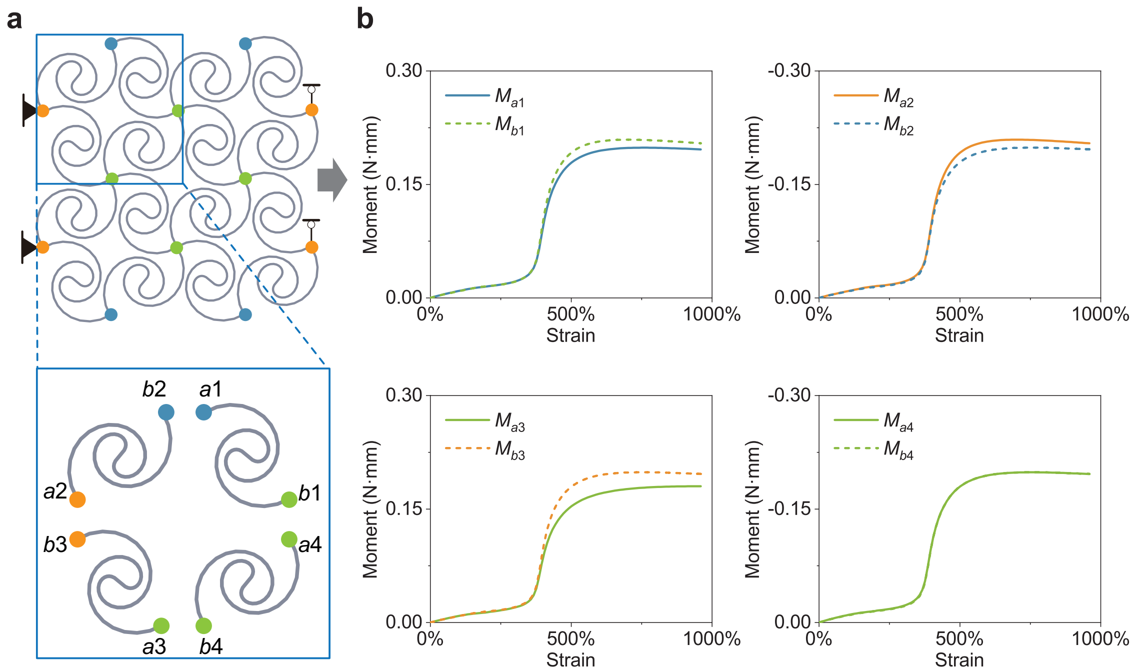

Figure S4: Mechanical behaviors under non-periodic boundary conditions. (a) Schematic of a typical unit in hyperelastic lattice metamaterials with non-periodic boundary conditions. (b) Relationship between applied moment on two ends of each microstructure and strain.

.

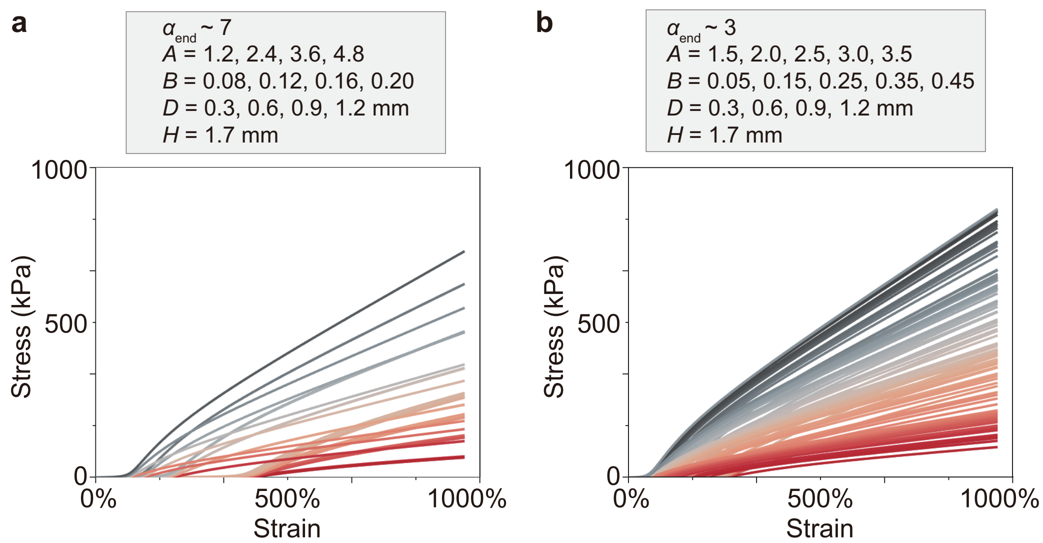

Figure S5: Databases of S-shaped stress-strain curves. Designs by modifying the parameters A and B in the curvature function $R(\alpha) = \alpha^A + 1/(\alpha+B)$ and the width D with (a) α_{end} ~7 and (b) α_{end} ~3.

.

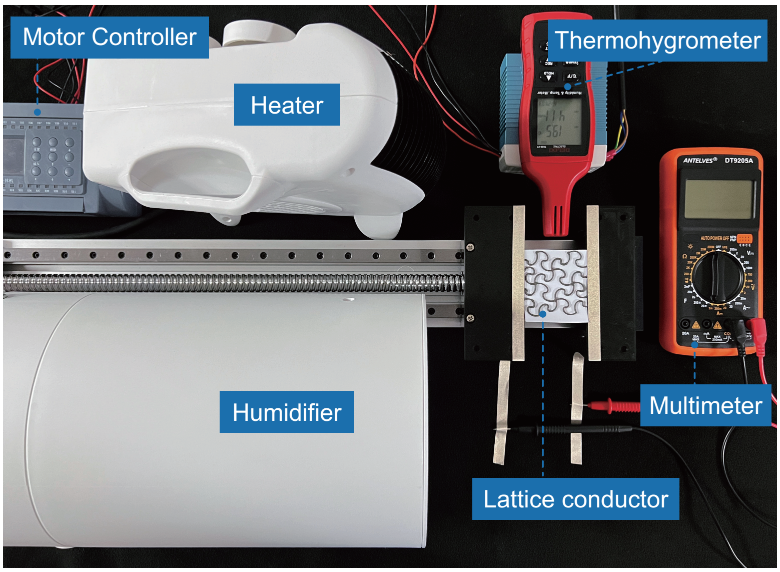

Figure S6: Experimental platform for measuring the resistance of lattice conductors under varying temperature and humidity conditions.

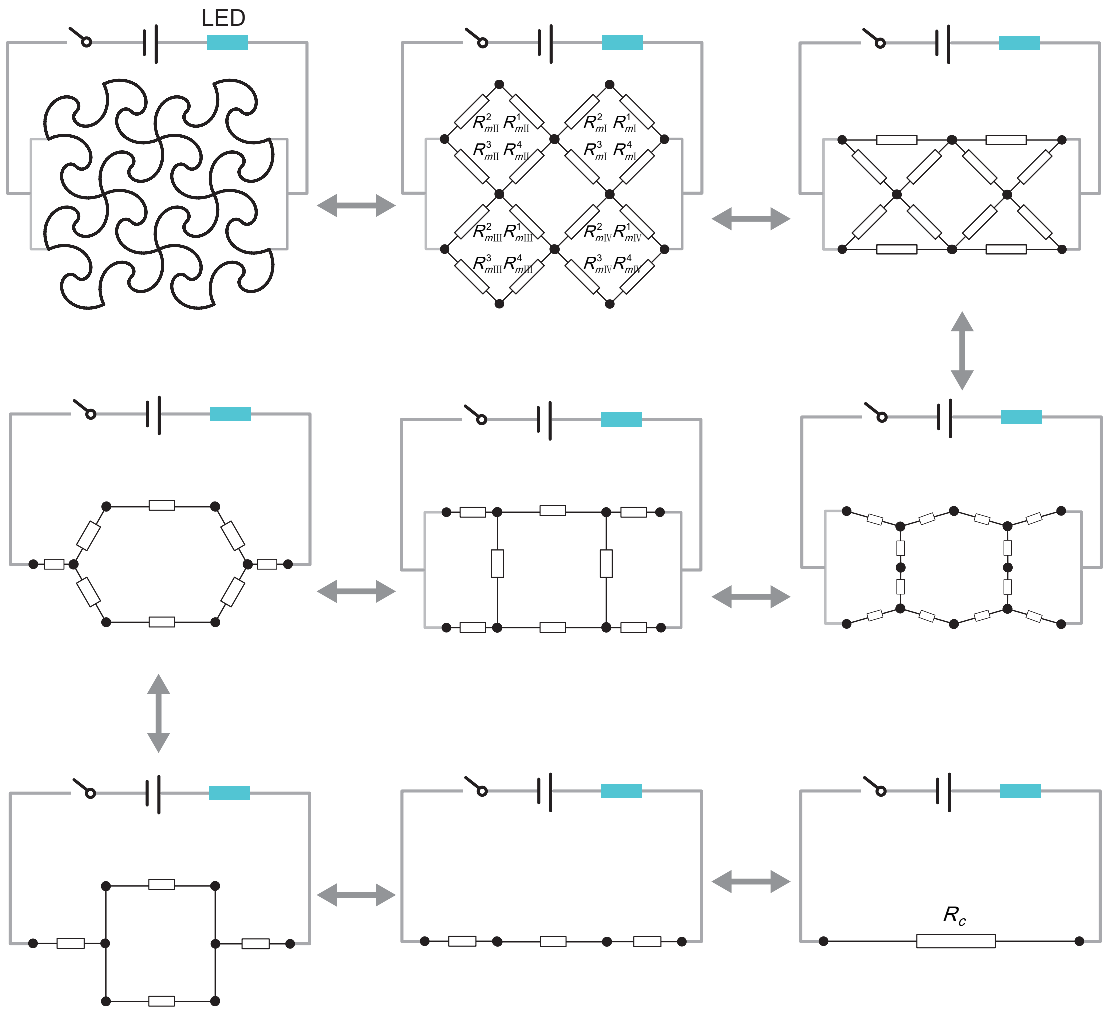

Figure S7: Calculation of circuit resistance. Based on Y-Δ transformation, the R_c is obtained by

$$R_c = F\left(\left\{R^i_{mj} \middle| i=1,\ 2,\ 3,\ 4; j=\mathrm{I},\ \mathrm{II},\ \mathrm{III},\ \mathrm{IV}\right\}\right) = \frac{(\Phi_3+\Phi_4+\Phi_6+\Phi_8)(\Phi_1+\Phi_2+\Phi_5+\Phi_7)}{\Phi_1+\Phi_2+\Phi_3+\Phi_4+\Phi_5+\Phi_6+\Phi_7+\Phi_8}$$

$$+\frac{R^1_{m\mathrm{III}}R^3_{m\mathrm{I}}\left(R^1_{m\mathrm{I}}+R^2_{m\mathrm{I}}\right)\left(R^3_{m\mathrm{III}}+R^4_{m\mathrm{III}}\right)}{\Phi_{11}\left(R^1_{m\mathrm{I}}+R^2_{m\mathrm{I}}+R^3_{m\mathrm{I}}+R^4_{m\mathrm{I}}\right)\left(R^1_{m\mathrm{III}}+R^2_{m\mathrm{III}}+R^3_{m\mathrm{III}}+R^4_{m\mathrm{III}}\right)}+\frac{R^2_{m\mathrm{IV}}R^4_{m\mathrm{II}}\left(R^1_{m\mathrm{II}}+R^2_{m\mathrm{II}}\right)\left(R^3_{m\mathrm{IV}}+R^4_{m\mathrm{IV}}\right)}{\Phi_9\left(R^1_{m\mathrm{II}}+R^2_{m\mathrm{II}}+R^3_{m\mathrm{II}}+R^4_{m\mathrm{II}}\right)\left(R^1_{m\mathrm{IV}}+R^2_{m\mathrm{IV}}+R^3_{m\mathrm{IV}}+R^4_{m\mathrm{IV}}\right)}$$

where $\Phi_1=\dfrac{R^2_{m\mathrm{III}}\left(R^3_{m\mathrm{III}}+R^4_{m\mathrm{III}}\right)}{R^1_{m\mathrm{III}}+R^2_{m\mathrm{III}}+R^3_{m\mathrm{III}}+R^4_{m\mathrm{III}}}$, $\Phi_2=\dfrac{R^1_{m\mathrm{IV}}\left(R^3_{m\mathrm{IV}}+R^4_{m\mathrm{IV}}\right)}{R^1_{m\mathrm{IV}}+R^2_{m\mathrm{IV}}+R^3_{m\mathrm{IV}}+R^4_{m\mathrm{IV}}}$, $\Phi_3=\dfrac{R^4_{m\mathrm{I}}\left(R^1_{m\mathrm{I}}+R^2_{m\mathrm{I}}\right)}{R^1_{m\mathrm{I}}+R^2_{m\mathrm{I}}+R^3_{m\mathrm{I}}+R^4_{m\mathrm{I}}}$, $\Phi_4=\dfrac{R^3_{m\mathrm{II}}\left(R^1_{m\mathrm{II}}+R^2_{m\mathrm{II}}\right)}{R^1_{m\mathrm{II}}+R^2_{m\mathrm{II}}+R^3_{m\mathrm{II}}+R^4_{m\mathrm{II}}}$,

$\Phi_5=\dfrac{R^2_{m\mathrm{IV}}\left(R^3_{m\mathrm{IV}}+R^4_{m\mathrm{IV}}\right)\Phi_{10}}{(R^1_{m\mathrm{IV}}+R^2_{m\mathrm{IV}}+R^3_{m\mathrm{IV}}+R^4_{m\mathrm{IV}})\Phi_9}$, $\Phi_6=\dfrac{R^4_{m\mathrm{II}}\left(R^1_{m\mathrm{II}}+R^2_{m\mathrm{II}}\right)\Phi_{10}}{(R^1_{m\mathrm{II}}+R^2_{m\mathrm{II}}+R^3_{m\mathrm{II}}+R^4_{m\mathrm{II}})\Phi_9}$, $\Phi_7=\dfrac{R^1_{m\mathrm{III}}\left(R^3_{m\mathrm{III}}+R^4_{m\mathrm{III}}\right)\Phi_3}{(R^1_{m\mathrm{III}}+R^2_{m\mathrm{III}}+R^3_{m\mathrm{III}}+R^4_{m\mathrm{III}})\Phi_{11}}$, $\Phi_8=\dfrac{R^3_{m\mathrm{I}}\left(R^1_{m\mathrm{I}}+R^2_{m\mathrm{I}}\right)\Phi_{12}}{\left(R^1_{m\mathrm{I}}+R^2_{m\mathrm{I}}+R^3_{m\mathrm{I}}+R^4_{m\mathrm{I}}\right)\Phi_{11}}$,

$\Phi_9=\dfrac{R^4_{m\mathrm{II}}\left(R^1_{m\mathrm{II}}+R^2_{m\mathrm{II}}+R^3_{m\mathrm{II}}\right)}{R^1_{m\mathrm{II}}+R^2_{m\mathrm{II}}+R^3_{m\mathrm{II}}+R^4_{m\mathrm{II}}}+\dfrac{R^2_{m\mathrm{IV}}\left(R^1_{m\mathrm{IV}}+R^3_{m\mathrm{IV}}+R^4_{m\mathrm{IV}}\right)}{R^1_{m\mathrm{IV}}+R^2_{m\mathrm{IV}}+R^3_{m\mathrm{IV}}+R^4_{m\mathrm{IV}}}$, $\Phi_{10}=\dfrac{R^3_{m\mathrm{II}}R^4_{m\mathrm{II}}}{R^1_{m\mathrm{II}}+R^2_{m\mathrm{II}}+R^3_{m\mathrm{II}}+R^4_{m\mathrm{II}}}+\dfrac{R^1_{m\mathrm{IV}}R^2_{m\mathrm{IV}}}{R^1_{m\mathrm{IV}}+R^2_{m\mathrm{IV}}+R^3_{m\mathrm{IV}}+R^4_{m\mathrm{IV}}}$,

$\Phi_{11}=\dfrac{R^3_{m\mathrm{I}}\left(R^1_{m\mathrm{I}}+R^2_{m\mathrm{I}}+R^4_{m\mathrm{I}}\right)}{R^1_{m\mathrm{I}}+R^2_{m\mathrm{I}}+R^3_{m\mathrm{I}}+R^4_{m\mathrm{I}}}+\dfrac{R^1_{m\mathrm{III}}\left(R^2_{m\mathrm{III}}+R^3_{m\mathrm{III}}+R^4_{m\mathrm{III}}\right)}{R^1_{m\mathrm{III}}+R^2_{m\mathrm{III}}+R^3_{m\mathrm{III}}+R^4_{m\mathrm{III}}}$ and $\Phi_{12}=\dfrac{R^3_{m\mathrm{I}}R^4_{m\mathrm{I}}}{R^1_{m\mathrm{I}}+R^2_{m\mathrm{I}}+R^3_{m\mathrm{I}}+R^4_{m\mathrm{I}}}+\dfrac{R^1_{m\mathrm{III}}R^2_{m\mathrm{III}}}{R^1_{m\mathrm{III}}+R^2_{m\mathrm{III}}+R^3_{m\mathrm{III}}+R^4_{m\mathrm{III}}}$.

.

Table S1. Comparison of theoretical models with existing studies

Ref.	Material hyperelasticity	Curve microstructures	Non-periodic boundary conditions
This work	√	√	√
[1]	√	×	×
[2]	√	×	×
[3]	√	×	√
[4]	√	×	√
[5]	×	√	×
[6]	×	√	×
[7]	×	√	×
[8]	×	√	×

√ The work considers this factor; × The work does not consider this factor.

Table S2. Comparison of sensor performance metrics with existing studies

Ref.	Bionic mechanics	High stretchability (over 300%)	Predictable electrical performance
This work	√	√	√
[9]	√	×	×
[10]	√	×	×
[11]	√	√	×
[12]	√	×	√
[13]	×	√	√
[14]	×	√	×
[15]	×	√	×
[16]	×	√	×

√ The work considers this factor; × The work does not consider this factor.

References

[1] Y. Zhang, K. Yu, K. H. Lee, K. Li, H. Du, Q. Wang, Mechanics of stretchy elastomer lattices, Journal of the Mechanics and Physics of Solids 159 (2022) 104782.

[2] G. L. Bluhm, O. Sigmund, F. Wang, K. Poulios, Nonlinear compressive stability of hyperelastic 2d lattices at finite volume fractions, Journal of the Mechanics and Physics of Solids 137 (2020) 103851.

[3] C. Perez-Garcia, J. Aranda-Ruiz, R. Zaera, D. Garcia-Gonzalez, Beam formulation and fe framework for architected structures under finite deformations, European Journal of Mechanics-A/Solids 96 (2022) 104706.

[4] J. Lotfi, S. Khalili, A. Damanpack, Micro-macro analysis of hyperelastic auxetic lattice structures under finite-strain regime, International Journal of Mechanical Sciences 274 (2024) 109246.

[5] Q. Ma, H. Cheng, K.-I. Jang, H. Luan, K.-C. Hwang, J. A. Rogers, Y. Huang, Y. Zhang, A nonlinear mechanics model of bio-inspired hierarchical lattice materials consisting of horseshoe microstructures, Journal of the Mechanics and Physics of Solids 90 (2016) 179–202.

[6] X. Xin, L. Liu, Y. Liu, J. Leng, 4d printing auxetic metamaterials with tunable, programmable, and reconfigurable mechanical properties, Advanced Functional Materials 30 (43) (2020) 2004226.

[7] J. Liu, D. Yan, Y. Zhang, Mechanics of unusual soft network materials with rotatable structural nodes, Journal of the Mechanics and Physics of Solids 146 (2021) 104210.

[8] Y. Yin, Z. Zhao, Y. Li, Theoretical and experimental research on anisotropic and nonlinear mechanics of periodic network materials, Journal of the Mechanics and Physics of Solids 152 (2021) 104458.

[9] K.-I. Jang, H. U. Chung, S. Xu, C. H. Lee, H. Luan, J. Jeong, H. Cheng, G.-T. Kim, S. Y. Han, J. W. Lee, et al., Soft network composite materials with deterministic and bio-inspired designs, Nature communications 6 (1) (2015) 6566.

[10] J. Park, S. Choi, A. H. Janardhan, S.-Y. Lee, S. Raut, J. Soares, K. Shin, S. Yang, C. Lee, K.-W. Kang, et al., Electromechanical cardioplasty using a wrapped elasto-conductive epicardial mesh, Science translational medicine 8 (344) (2016) 344ra86–344ra86.

[11] X. Qu, S. Wang, Y. Zhao, H. Huang, Q. Wang, J. Shao, W. Wang, X. Dong, Skin-inspired highly stretchable, tough and adhesive hydrogels for tissue-attached sensor, Chemical Engineering Journal 425 (2021) 131523.

[12] Y. Deng, X. Guo, Y. Lin, Z. Huang, Y. Li, Dual-phase inspired soft electronic sensors with programmable and tunable mechanical properties, ACS nano 17 (7) (2023) 6423–6434.

[13] T. Li, Y. Jiang, K. Yu, Q. Wang, Stretchable 3d lattice conductors, Soft Matter 13 (42) (2017) 7731–7739.

[14] Y. Xiao, C. Lu, Z. Yu, Y. Lian, Y. Ma, Z. Chen, X. Jiang, Y. Zhang, Transparent, high stretchable, environmental tolerance, and excellent sensitivity hydrogel for flexible sensors and capacitive pens, ACS Applied Materials & Interfaces 15 (37) (2023) 44280–44293.

[15] Q. Xia, W. Li, X. Zou, S. Zheng, Z. Liu, L. Li, F. Yan, Metal–organic framework (mof) facilitated highly stretchable and fatigue-resistant ionogels for recyclable sensors, Materials Horizons 9 (11) (2022) 2881–2892.

[16] Z. Shen, Z. Zhang, N. Zhang, J. Li, P. Zhou, F. Hu, Y. Rong, B. Lu, G. Gu, High-stretchability, ultralow-hysteresis conductingpolymer hydrogel strain sensors for soft machines, Advanced Materials 34 (32) (2022) 2203650.